

Suppressed CO emission and high G/D ratios in z = 2 galaxies with sub-solar gas-phase metallicity

R. T. Coogan, M. T. Sargent, E. Daddi, F. Valentino, V. Strazzullo, M. Béthermin, R. Gobat, D. Liu, G. Magdis

▶ **To cite this version:**

R. T. Coogan, M. T. Sargent, E. Daddi, F. Valentino, V. Strazzullo, et al.. Suppressed CO emission and high G/D ratios in z = 2 galaxies with sub-solar gas-phase metallicity. Monthly Notices of the Royal Astronomical Society, 2019, 485, pp.2092-2105. 10.1093/mnras/stz409 . insu-03666750

HAL Id: insu-03666750

https://insu.hal.science/insu-03666750

Submitted on 13 May 2022

HAL is a multi-disciplinary open access archive for the deposit and dissemination of scientific research documents, whether they are published or not. The documents may come from teaching and research institutions in France or abroad, or from public or private research centers.

L'archive ouverte pluridisciplinaire **HAL**, est destinée au dépôt et à la diffusion de documents scientifiques de niveau recherche, publiés ou non, émanant des établissements d'enseignement et de recherche français ou étrangers, des laboratoires publics ou privés.

Monthly Notices of the ROYAL ASTRONOMICAL SOCIETY

MNRAS **485,** 2092–2105 (2019) doi:10.1093/mnras/stz409
Advance Access publication 2019 February 11

Suppressed CO emission and high G/D ratios in $z = 2$ galaxies with sub-solar gas-phase metallicity

R. T. Coogan [1,2★] M. T. Sargent [1] E. Daddi [2] F. Valentino [3] V. Strazzullo,[4] M. Béthermin,[5,6] R. Gobat,[7] D. Liu[8] and G. Magdis[3,9]

[1]*Astronomy Centre, Department of Physics and Astronomy, University of Sussex, Brighton BN1 9QH, UK*
[2]*CEA, IRFU, DAp, AIM, Université Paris-Saclay, Université Paris Diderot, Sorbonne Paris Cité, CNRS, F-91191 Gif-sur-Yvette, France*
[3]*Cosmic Dawn Center, Niels Bohr Institute, University of Copenhagen, Juliane Mariesvej 30, DK-2100 Copenhagen, Denmark*
[4]*Department of Physics, Ludwig-Maximilians-Universitat, Scheinerstr 1, D-81679 Munchen, Germany*
[5]*Aix Marseille Univ, CNRS, LAM, Laboratoire d'Astrophysique de Marseille, Marseille, France*
[6]*European Southern Observatory, Karl-Schwarzschild-Str 2, D-85748 Garching, Germany*
[7]*Instituto de Física, Pontificia Universidad Católica de Valparaíso, Casilla 4059, Valparaíso, Chile*
[8]*Max Planck Institute for Astronomy, Konigstuhl 17, D-69117 Heidelberg, Germany*
[9]*Institute for Astronomy, Astrophysics, Space Applications and Remote Sensing, National Observatory of Athens, 15236 Athens, Greece*

Accepted 2019 January 17. Received 2018 December 22; in original form 2018 September 1

ABSTRACT

We study a population of significantly sub-solar enrichment galaxies at $z = 1.99$, to investigate how molecular gas, dust, and star formation relate in low-metallicity galaxies at the peak epoch of star formation. We target our sample with several deep Atacama Large Millimeter/submillimeter Array and Very Large Array datasets, and find no individual detections of CO[4–3], CO[1–0], or dust, in stark contrast to the >60 per cent detection rate expected for solar-enrichment galaxies with these MS Hα star formation rates (SFRs). We find that both low- and high-density molecular gas (traced by CO[1–0] and CO[4–3], respectively) are affected by the low enrichment, showing sample average (stacked) luminosity deficits >0.5–0.7 dex below expectations. This is particularly pertinent for the use of high-J CO emission as a proxy of instantaneous SFR. Our individual galaxy data and stacked constraints point to a strong inverse dependence $\propto Z'^{\gamma}$ of gas-to-dust ratios (G/D) and CO-to-H_2 conversion factors (α_{CO}) on metallicity at $z \sim 2$, with $\gamma_{G/D} < -2.2$ and $\gamma_{\alpha_{CO}} < -0.8$, respectively. We quantify the importance of comparing G/D and α_{CO} versus metallicity trends from the literature on a common, suitably normalized metallicity scale. When accounting for systematic offsets between different metallicity scales, our $z \sim 2$ constraints on these scaling relations are consistent with the corresponding relations for local galaxies. However, among those local relations, we favour those with a steep/double power-law dependence of G/D on metallicity. Finally, we discuss the implications of these findings for (a) gas mass measurements for sub-M^* galaxies, and (b) efforts to identify the characteristic galaxy mass scale contributing most to the comoving molecular gas density at $z = 2$.

Key words: galaxies: abundances – galaxies: evolution – galaxies: high-redshift – galaxies: ISM – galaxies: star formation.

1 INTRODUCTION

Our current understanding of galaxy properties at the peak epoch of star formation ($z \sim 2$), in particular the interstellar medium (ISM), is primarily driven by observations of the brightest, most massive galaxies. The interplay between gas, dust, and star formation for the 'normal' galaxy population with $M_\star \sim 10^{10}$–10^{11} $M_\odot$ and approximately solar enrichment at $z = 2$ is now reasonably well characterized (e.g. Aravena et al. 2010; Daddi et al. 2010a,b; Genzel et al. 2010; Magdis et al. 2012; Tacconi et al. 2013, 2018; Santini et al. 2014; Sargent et al. 2014; Scoville et al. 2014, 2017; Tan et al. 2014; Decarli et al. 2016). However, the ISM properties of lower mass galaxies at this redshift are much less well-understood, despite the fact that they are far more numerous than higher mass systems. This gap in our knowledge is a consequence of sub-M^* galaxies

★ E-mail: r.coogan@sussex.ac.uk

© 2019 The Author(s)
Published by Oxford University Press on behalf of the Royal Astronomical Society

Downloaded from https://academic.oup.com/mnras/article/485/2/2092/5315777 by guest on 13 May 2022

being much more difficult to observe, in part due to their relative faintness. It is however important to push down to these systems to improve our understanding of the gas cycle and consumption across a broad range of halo and stellar masses.

A compounding difficulty in ISM observations is due to the low gas-phase metal abundance in these systems, as described by the 'mass−metallicity relation' (MZR), both in the local Universe and at higher redshifts (e.g. Tremonti et al. 2004; Zahid et al. 2014). The low enrichment of these galaxies affects quantities commonly used to estimate ISM content from observational data, such as the gas-to-dust ratio (G/D) and CO-to-H_2 conversion factor (α_{CO}). Molecular gas masses can be estimated from observations through CO spectroscopy, using α_{CO} to convert between CO luminosity and molecular gas mass. However, at low oxygen abundance, increasing proportions of star formation in a galaxy are predicted to occur in 'CO-dark' molecular Hydrogen gas (e.g. Israel 1997; Grenier, Casandjian & Terrier 2005; Wolfire, Hollenbach & McKee 2010). At low metallicity, the shielding of CO molecules by dust molecules is reduced, leading to higher photodissociation of CO molecules by ultraviolet (UV) radiation and a lower CO emission per unit molecular gas mass, thus increasing the value of α_{CO}.

In addition to this intrinsic lack of CO, the low-J CO transitions become observationally too faint with increasing redshift, and many low-J transitions fall out of suitable observing windows. It is therefore more practical to use sensitive instruments such as the Atacama Large Millimeter/submillimeter Array (ALMA) to detect emission from the higher order transitions of CO. An excitation correction is then applied, thereby adding further assumptions to the task of measuring molecular gas masses. Alternatively, gas masses can be inferred through cold dust continuum observations. This is done by relating the dust emission to the total gas mass through the G/D ratio (e.g. Guelin et al. 1993; Corbelli et al. 2012; Eales et al. 2012; Magdis et al. 2012; Bourne et al. 2013; Scoville et al. 2014; Groves et al. 2015), which is again closely linked to the metallicity of a galaxy.

Previous studies have therefore largely focused on characterizing the relationship between gas, dust, and metallicity of the ISM in local galaxies (e.g. Burstein & Heiles 1982; Issa, MacLaren & Wolfendale 1990; Draine et al. 2007; Leroy et al. 2011; Magdis et al. 2012; Sandstrom et al. 2013; Rémy-Ruyer et al. 2014; Tan et al. 2014; Belfiore et al. 2015; Amorín et al. 2016). These works have illustrated a clear inverse dependence of G/D and α_{CO} on metallicity. However, observations of the high-redshift, low-metallicity regime are now required, in order to investigate whether similar relations as observed at low redshift also hold for galaxies in the peak epoch of galaxy formation. With the lack of equivalent information at high redshift, we are currently forced to either assume no metallicity dependence when deriving gas content from continuum or line observations at high redshift, or to assume that the scaling relations calibrated locally are valid at higher redshift. Some early attempts have been made to constrain these scaling relations at high redshift, such as those by Genzel et al. (2012) and Saintonge et al. (2013). Genzel et al. (2012) used the CO[3–2] and CO[2–1] transitions to perform a study of normal star-forming galaxies between $z \sim 1$ and 2, with stellar mass $M_\star \gtrsim 10^{10}\,M_\odot$ and oxygen abundance on the Denicoló, Terlevich & Terlevich (2002, D02) scale of 8.4–8.9. They found a strong inverse dependence of α_{CO} on metallicity in star-forming galaxies at $z > 1$, similar to what is observed at $z \sim 0$. Saintonge et al. (2013) study the relationship between G/D and metallicity using $\sim 10^{10}\,M_\odot$ $z > 2$ lensed galaxies over a similar metallicity range, and find an increase in the normalization of the G/D ratio a factor 1.7 above the relation found for $z = 0$ galaxies, suggesting an evolution of the G/D ratio with redshift as well as metallicity. By constraining these scaling relations at lower metallicities, we will be able to more accurately use observations to characterize the properties of these galaxies, such as their star formation efficiencies and molecular gas content.

In this paper, we study the relationship between metallicity, gas, star formation, and dust content, in a sample of sub-solar metallicity galaxies in the cluster Cl J1449+0856 at $z = 1.99$ (Gobat et al. 2011). Despite residing in a cluster environment, these galaxies are consistent with the MZR at $z = 2$ (as discussed in Section 3.1) as well as the upper half of the main sequence (MS) of star formation (Section 2.3), and are in this sense representative of the 'normal' population of galaxies for the purposes of this work. The study of these galaxies therefore allows us rare insight into the physics of the numerous sub-solar enrichment galaxies at this redshift, at masses lower than the characteristic mass of the stellar mass function at $z = 2$ ($\log_{10}(M^*/M_\odot) \sim 10.4$; see also Ilbert et al. 2010, 2013; Tomczak et al. 2014; Davidzon et al. 2017). We target the CO[4–3] and CO[1–0] transitions in our galaxies, in addition to the dust continuum emission at 870 μm and 2 mm. We describe our observations and data reduction in Section 2, and present our stacked gas and dust constraints in Section 3. We discuss the implications of our results in the context of L'_{CO}–star formation rate (SFR) correlations, as well as scaling relations between α_{CO} and G/D with metallicity in Section 4. We summarize in Section 5. Throughout this paper we use a ΛCDM cosmology with $H_0 = 70\,km s^{-1}\,Mpc^{-1}$, $\Omega_M = 0.3$, and $\Omega_\Lambda = 0.7$. We adopt a Chabrier initial mass function (Chabrier 2003).

2 SAMPLE SELECTION AND MAIN DATA SETS

The spectroscopically confirmed galaxy population of Cl J1449+0856 has been studied at many different wavelengths to date, spanning X-ray to radio observations (Gobat et al. 2011, 2013; Strazzullo et al. 2013, 2016; Valentino et al. 2015, 2016; Coogan et al. 2018; Strazzullo et al. 2018). A subset of the ∼30 confirmed cluster members were selected for Subaru/Multi-object InfraRed Camera and Spectrograph (MOIRCS) near-infrared (IR) follow-up in Valentino et al. (2015, V15), based on their spectroscopic WFC3 redshifts (Gobat et al. 2013), and their star-forming *UVJ* colours (Strazzullo et al. 2013). Seven of these targeted star-forming members were detected by MOIRCS, as were two galaxies known to host X-ray active galactic nuclei (AGNs; Gobat et al. 2013). We exclude these AGNs from our analyses, as the ionizing radiation from the AGN is known to alter line ratios compared to pure star-forming galaxies (as demonstrated by e.g. the BPT diagram, Kewley et al. 2013), rendering metallicity estimates unreliable. Here, we discuss the five of these seven star-forming galaxies for which we also have follow-up ALMA and Very Large Array (VLA) observations, allowing us to probe their ISM properties.

A colour image of the cluster is shown in Fig. 1, alongside cut-outs of the cluster members discussed here. As shown in V15, these galaxies extend from the core of the cluster towards the outskirts, reaching $\sim R_{200}$ of Cl J1449+0856 at a physical radius of ∼0.4 Mpc. The cores of these galaxies do not appear highly dust obscured at rest-frame optical wavelengths, demonstrated by their blue colours in Fig. 1, implying ongoing star formation activity.

To study the dust and molecular gas content of our targets, we use the ALMA and VLA data described in Coogan et al. (2018): CO[4–3] line and 2 mm continuum fluxes were derived from ALMA band 4 data, CO[1–0] line fluxes from VLA *Ka*-band observations and 870 μm continuum measurements from ALMA band 7 images.

Downloaded from https://academic.oup.com/mnras/article/485/2/2092/5315777 by guest on 13 May 2022

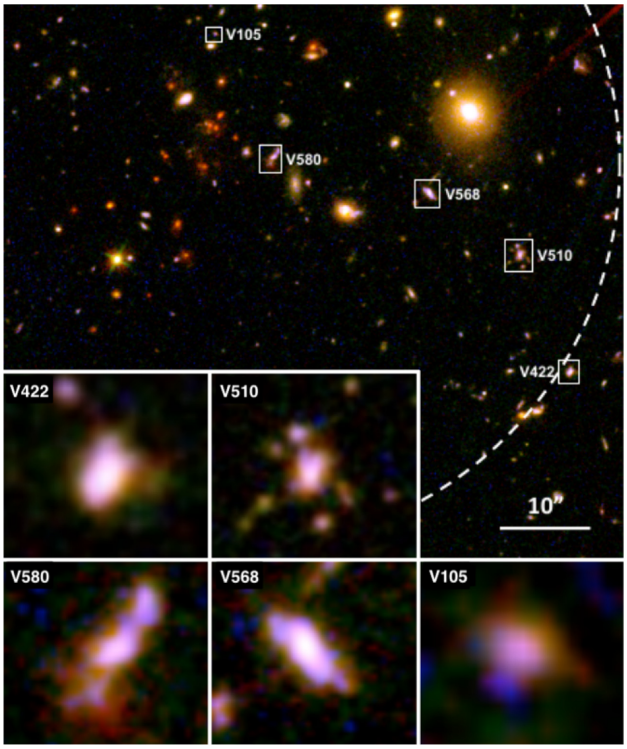


Figure 1. Colour image of the galaxy cluster Cl J1449+0856, using *HST*/WFC3 filters *F606W*, *F105W*, and *F140W*. The five low gas-phase metallicity galaxies discussed in this paper are indicated by white rectangles, and labelled with their IDs. The scale at the bottom right corner gives the angular scale of the main image, the cut-outs are zoomed versions of the individual galaxies as indicated. The white dashed circle shows the cluster $R_{200} \sim 0.4$ Mpc physical radius (Gobat et al. 2013).

2.1 MOIRCS observations

Our five star-forming galaxies were selected as part of a MOIRCS near-IR spectroscopic follow-up, for which the observations and data reduction are described in detail in V15. Each galaxy was observed through a HK500 grism slit of width 0.7 arcsec, and the data were reduced using the MCSMDP pipeline (Yoshikawa et al. 2010). These observations primarily measured the [N II]6548, [N II]6583, [O III]5007, and Hα emission lines, in order to derive metallicities, precise spectroscopic redshifts, and Hα SFRs. For galaxy V105, not presented in V15 but discussed in this paper, the same approach as in V15 was taken for deriving these quantities. The results of these measurements are listed in Tables 1 and 3.

2.2 CO spectroscopy and dust continuum measurements

The ALMA band 4 data used to measure CO[4–3] fluxes contain a deeper, core observation (continuum root-mean-squared (RMS) noise 8 μJy beam^{-1}), and a shallower pointing (continuum RMS 24 μJy beam^{-1}) of the outskirts of the cluster. The VLA *Ka*-band data used to measure CO[1–0] emission in the galaxies is a single pointing with continuum RMS 3 μJy beam^{-1}.

We extracted CO spectra at fixed positions, corresponding to the rest-frame optical positions of the galaxies shown in Fig. 1. Line fluxes were measured directly in the uv-visibility plane with the GILDAS[1] task `uv_fit`. Visibilities were collapsed over the expected CO linewidth, chosen to correspond to the velocity range containing 90 per cent of the Hα line flux, using the individual Hα linewidths listed in Table 3. It should be noted that these listed 90 per cent-flux linewidths, $W_{90\%}$, are full width zero power (FWZP) widths, whereas the Hα linewidths are Gaussian full width half maxima (FWHM). The choice of line profile is not expected to have a significant effect on our line flux measurements, as the fluxes are measured directly in the collapsed visibility data over the given velocity width. Additionally, the line FWHM for detected CO[4–3] transitions of other members of Cl J1449+0856 were found to be consistent between a double and a single Gaussian profile in Coogan et al. (2018). Due to the small optical sizes of the galaxies (see Fig. 1) compared with the size of the beams for the CO datasets (1.19 arcsec × 0.96 arcsec and 0.70 arcsec × 0.64 arcsec for CO[4–3] and CO[1–0], respectively), as well as the low SNR achieved by the individual CO spectra, all spectra were extracted assuming a point spread function (PSF) response (1σ spectral noise over a 100 km s^{-1} width was 10 and 4 mJy km s^{-1} for the CO[4–3] core pointing and CO[1–0], respectively). In order to avoid contamination from other galaxies, particularly in the cluster core, neighbouring galaxies were iteratively modelled with GILDAS and removed from the data, before measuring the properties of the low-metallicity galaxy population. The exception to this was galaxy V580, which was modelled simultaneously with its dusty companion (galaxy ID A2 in Coogan et al. 2018).

2 mm continuum fluxes were measured in the uv-plane, after collapsing the data over the line-free spectral windows. The 870 μm map is a mosaic formed of seven single pointings, with a total area of 0.3 arcmin^2 centred on the cluster core. This therefore only covers the positions of galaxies V105, V580, and V568. However, we include this dataset in the analysis for these three galaxies (as well as the stacked sample) as it leads to a significant improvement in sensitivity of the dust emission maps (×2 compared to the 2 mm continuum). Continuum fluxes in the 870 μm map were extracted using the software GALFIT (Peng 2010), using the full dirty beam on the dirty, calibrated images, as the mosaic format made the transportation into GILDAS format impractical. We have previously verified that continuum fluxes measured with Common Astronomy Software Applications (McMullin et al. 2007), GILDAS and GALFIT for the dusty star-forming galaxies in this cluster are consistent (Coogan et al. 2018). All galaxies in our sample were again modelled as PSFs in the continuum (beams of 1.19 arcsec × 0.96 arcsec and 1.41 arcsec × 0.62 arcsec for 2 mm and 870 μm, respectively).

2.3 SED fitting and star formation rates

We take stellar masses and SFRs for our sample as derived by Strazzullo et al. (2016), using Fitting and Assessment of Synthetic Templates (Kriek et al. 2009) spectral energy distribution (SED) modelling. Continuum reddening values were calculated assuming a truncated star formation history before correction to the higher nebular extinction, as is appropriate for the Hα-derived SFRs (e.g. Calzetti et al. 2000; Kashino et al. 2013; Pannella, Elbaz & Daddi 2013; V15). The updated reddening values from Strazzullo et al. (2016) resulted in reductions of the galaxy stellar masses and Hα SFRs by ∼0.4 and ∼0.2 dex, respectively, compared with V15. The nebular $E(B-V)$ values and Hα SFRs are presented in Table 1. These galaxies have $\delta_{\rm MS} = {\rm SFR}_{\rm H\alpha}/{\rm SFR}_{\rm MS}$ values between 0.08 and 1.1 dex, as shown in Table 1. The median offset of our galaxies from the MS is 1.6σ, where all but one of the galaxies (V422) lie below the frequently adopted 'cut-off' between the starburst

[1] http://www.iram.fr/IRAMFR/GILDAS

Downloaded from https://academic.oup.com/mnras/article/485/2/2092/5315777 by guest on 13 May 2022

Table 1. Physical properties of the five low-metallicity cluster galaxies, and their average properties. MOIRCS rest-frame optical spectroscopic redshifts are from V15. [N II] was individually undetected in all galaxies except V422, so 2σ upper limits on the oxygen abundance are shown, based on the N2 = $\log_{10}$([N II]/H α) diagnostic and the PP04 calibration. The characteristic metallicity of the sample was derived from a weighted stack, see Section 3.1 for details. δ_{MS} and δ_{MZR} are the logarithmic offsets from the MS of star formation (Sargent et al. 2014) and the MZR (Zahid et al. 2014), respectively (a negative value indicates an offset below the relations). The characteristic mass of the sample is the average of the five individual stellar mass estimates. H α SFRs, UV SFRs, and the nebular reddening values (used to derive the dust-corrected H α SFRs given) are also reported. The UV SFRs were calculated using continuum reddening. 3σ upper limits on UV SFR are shown. The characteristic H α and UV SFR values of the sample are the medians of the individual SFRs.

ID	RA (deg)	Dec. (deg)	z_{opt} –	12 + log(O/H) PP04	$\log_{10}(M_\star)$ $\log_{10}(M_\odot)$	δ_{MZR} (dex)	δ_{MS} (dex)	$SFR_{H\alpha}$ ($M_\odot$ yr^{-1})	SFR_{UV} ($M_\odot$ yr^{-1})	$E(B-V)_{neb}$ (mag)
V568	222.302 42	8.938 74	1.987 ± 0.001	<8.26	9.66 ± 0.30	< −0.03	0.52	39 ± 5	41 ± 8	0.15
V580	222.307 02	8.939 78	2.001 ± 0.001	<8.48	10.06 ± 0.30	<0.06	0.34	53 ± 10	31 ± 8	0.20
V422	222.298 23	8.933 51	1.988 ± 0.001	8.14 ± 0.12	9.76 ± 0.30	–0.18	1.1	170 ± 23	71 ± 13	0.37
V510	222.299 72	8.93691	1.988 ± 0.001	<8.34	9.86 ± 0.30	< −0.01	0.49	52 ± 8	57 ± 10	0.35
V105	222.308 73	8.943 40	1.988 ± 0.001	<8.59	9.16 ± 0.30	<0.42	0.08	6 ± 2	<19	0.37
Sample Ave.	–	–	1.9904	8.34 ± 0.13	9.79 ± 0.13	0.01	0.49	52^{+19}_{-11}	41 ± 9	–

and MS regimes, at 0.6 dex (Rodighiero et al. 2011; Sargent et al. 2012).

3 RESULTS

In this section we describe our metallicity measurements, CO[1–0] and CO[4–3] line fluxes, dust continuum measurements, and estimates for the molecular gas masses of our targets. CO fluxes are used to examine the relationship between CO luminosity and SFR in the low-metallicity regime. The combination of gas mass and $L'_{CO[1-0]}$ allows us to put constraints on the α_{CO} conversion factor, and similarly, we can use the dust continuum measurements to constrain G/D ratios.

3.1 Gas-phase metallicity measurements

We derive oxygen abundances with the N2 = $\log_{10}$([N II]6583/H α) diagnostic and the Pettini & Pagel (2004, PP04) calibration using the MOIRCS spectra of our targets. Significant (SNR > 5) H α line detections were found for all five galaxies, but [N II] remained undetected with the exception of V422 where we find a weak detection (2.0σ). We therefore derived upper limits on the metallicities of the [N II]-undetected galaxies. Known disadvantages of the N2 calibration are that it saturates at high metallicity, as well as being dependent on both the ionization parameter and the ratio of N/O (Baldwin, Phillips & Terlevich 1981; Kewley & Dopita 2002; Pérez-Montero & Contini 2009). However, our galaxies are at significantly sub-solar metallicity, and the effect of the varying N/O ratio on the derived metallicities of these galaxies is negligible (V15). To further verify our N2-based metallicity values, we also use the O3N2 PP04 calibration to calculate metallicities of these galaxies, again using the MOIRCS data. We find that the O3N2 indicator gives systematically lower metallicity than N2, as has also been seen at high-z by several other studies (e.g. Erb et al. 2006, Steidel et al. 2014; Zahid et al. 2014). We find a median metallicity offset between the metallicity upper limits inferred with N2 and O3N2 respectively of 0.09 dex, within the systematic uncertainties of the two estimators (0.18 and 0.14 dex, for N2 and O3N2 respectively, PP04). We use N2 as our primary metallicity estimator, allowing us to make direct comparisons with the relevant literature (e.g. Magdis et al. 2011, 2012; V15).

We report the metallicities of the individual galaxies in Table 1, as well as the offsets from the MZR at $z \sim 2$. For the higher mass galaxies, with $M_\star > 10^{9.6}\,M_\odot$, their metallicity constraints place them ∼0.02 dex below the expected value, based on the mass–metallicity relation at $z = 2$ (Zahid et al. 2014). For V105, the galaxy with the lowest SFR and stellar mass, the upper limit on the oxygen abundance places it ∼0.4 dex above the MZR.[2] The offsets δ_{MZR} calculated with respect to the parametrization of the MZR in Zahid et al. (2014) are consistent with those we derive for the MZR in both the N2 and O3N2 PP04 calibrations, as reported by Steidel et al. (2014).

We derived a stacked metallicity estimate for all five galaxies combined. Following the same procedure as in V15, the continuum, H α, [N II]6548 and [N II]6583 lines were modelled simultaneously in the stacked spectrum, using 1D Gaussian profiles. We imposed the positions of the [N II] lines to correspond to the redshift derived from the H α line, as it has the highest SNR. We also imposed the standard constraint that the ratio of the line fluxes between the two [N II] lines must be equal to 3.05 (Storey & Zeippen 2000). The amplitude of a frequency-independent continuum contribution was left free to vary. We verified through a jackknifing analysis that our results are not heavily biased by individual galaxies, and that the method of stacking (optimal, median, average) does not significantly affect our results. The average metallicity and associated error we quote for the stacked galaxies is based on a Monte Carlo resampling, for which we created 1000 stacked spectra, each composed of a weighted average of individual, resampled galaxy spectra.

We find a weighted-average, stacked metallicity value $Z = 8.34 \pm 0.13$. This error includes an additional factor derived from the spread of the metallicities from the jackknifing analysis, without the systematic uncertainty on the N2 PP04 calibration itself (0.18 dex). V15 used a sample of six low-metallicity cluster galaxies (four of which are common to this study, with the exception of V105), to derive a mean metallicity value of $Z = 8.261 \pm 0.083$, consistent with what we find for our sample. With an average mass $\log_{10}(M_\star/M_\odot) = 9.79 \pm 0.30$, this stacked metallicity measurement implies an offset of ∼0.01 dex above the Zahid et al. (2014) MZR (the mean offset δ_{MZR} with respect to the Steidel et al. (2014) MZR at $z = 2.3$ is −0.03 dex, consistent within 0.2σ).

[2]Note that 4/5 of our galaxies were reported as lying below the $z = 2$ MZR in V15. It is the reduction of the stellar masses, discussed in Section 2.3, that brings these galaxies into agreement with the MZR (whilst metallicity values remain the same).

Downloaded from https://academic.oup.com/mnras/article/485/2/2092/5315777 by guest on 13 May 2022

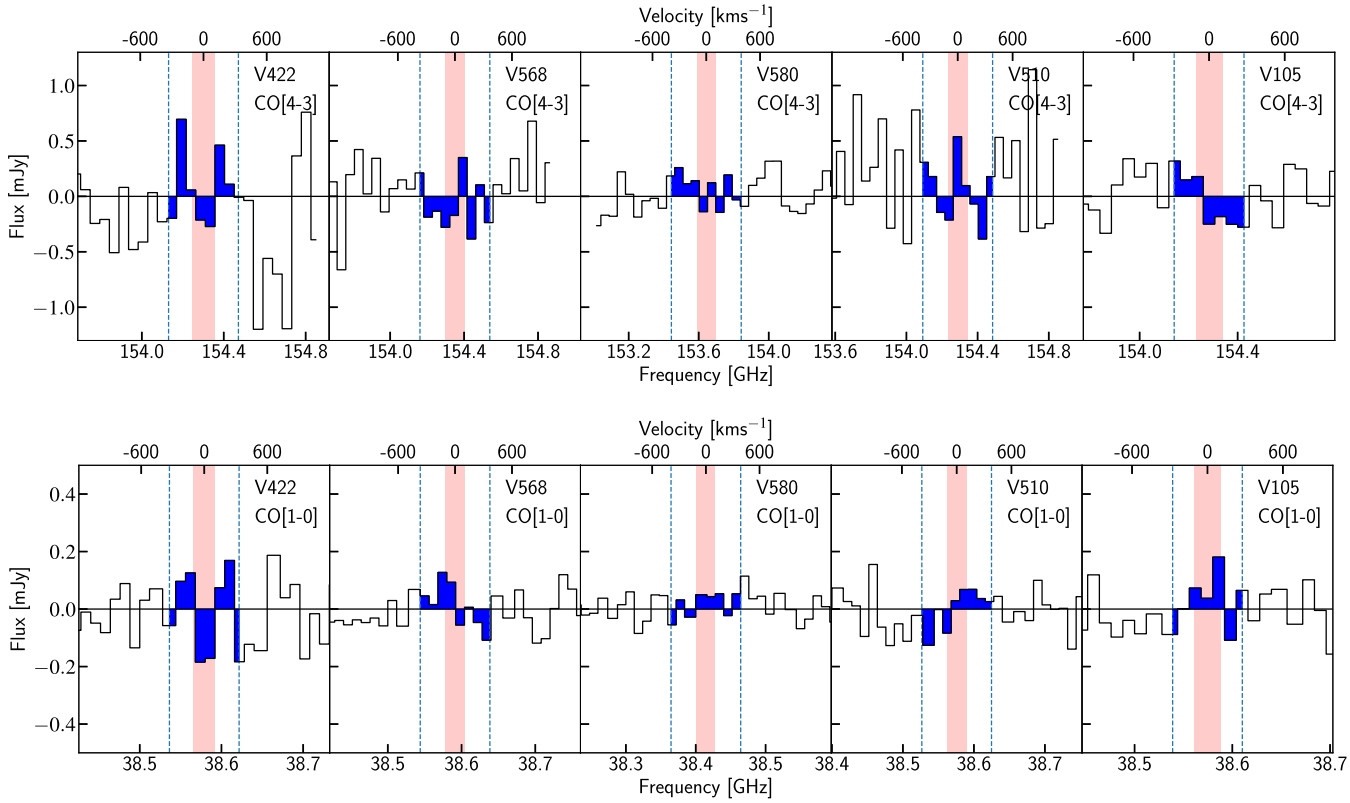


Figure 2. Top panel (lower panel): individual CO[4–3] (CO[1–0]) spectra binned into 90 km s^{-1} channels. The expected central position of the CO lines based on optical spectroscopic redshifts and associated errors are shown by the red vertical bands. The expected widths of the CO lines are shown by the blue shading of the spectra and the vertical dashed lines. The CO[4–3] and CO[1–0] transitions of all galaxies are individually undetected.

Table 2. Integrated line fluxes of the galaxies at the expected positions of the CO[4–3] and CO[1–0] lines, taken over the 90 per cent flux widths shown in Table 3, $W_{90\%}$. Continuum upper limits at 870 μm and 2 mm are also shown. 3σ upper limits are given. A dashed entry for a galaxy indicates that the galaxy was not covered by the 870 μm mosaic. We do not give a sample average 870 μm flux, as not all galaxies are present in the 870 μm data.

ID	$I_{\rm CO[4-3]}$ (mJy km s^{-1})	$I_{\rm CO[1-0]}$ (mJy kms^{-1})	$F_{870\,\mu\rm m}$ (μJy)	$F_{2\,\rm mm}$ (μJy)
V568	<118	<39	<346	<32
V580	<74	<38	<203	<22
V422	<221	<79	–	<57
V510	<218	<58	–	<58
V105	<89	<31	<239	<30
Sample Ave.	<47	<20	–	<14

3.2 Molecular line emission: CO[1–0] and CO[4–3]

As discussed in Section 2, by using the galaxy optical redshifts and the Hα linewidths, we can extract CO spectra and line fluxes for each galaxy over the expected velocity range. The CO[4–3] spectra for the individual galaxies are displayed in the top panel of Fig. 2 and show no significant line detections. Similarly, the galaxies in our sample also remain individually undetected in the CO[1–0] transition (Fig. 2, lower panel). Upper limits for all line fluxes are presented in Table 2. We perform a weighted mean stack of all five galaxies (Fig. 3), and calculate the stacked line fluxes over the mean FWZP linewidth of the individual galaxies, Δv = 753 ± 22 km s^{-1}. This corresponds to the weighted mean linewidth ($\langle\sigma_{\rm H\alpha}\rangle$ = 231 km s^{-1}), transformed to an FWZP containing 90 per cent of the Hα flux. The error on this average linewidth reflects the error on the weighted mean. We perform Monte Carlo Markov Chain simulations to take into account the statistical errors on the redshifts of the individual spectra, displacing the individual spectra before stacking, according to the redshift sampled from a Gaussian distribution. The effect of this on the output stacked line fluxes is negligible. The flux uncertainties on the stacked spectra have been calculated using standard error propagation on the weighted mean of the individual channels. We verify that the error on the flux arising from the error on the linewidth is negligible, using a resampling approach over a Gaussian linewidth distribution. It should also be noted that the upper limits on these CO line fluxes are proportional to the square root of the linewidth. A factor of two difference in linewidth, for example, would therefore alter the derived (logarithmic) CO luminosities by ±0.15 dex, and would not affect the conclusions of this work.

We find no detection of CO[4–3] emission, even in this stacked data, where the noise on the stacked spectrum is reduced by a factor $\sim\sqrt{5}$ compared to the individual spectra. We therefore place a 3σ upper limit on the stacked CO[4–3] line flux of <47mJy kms^{-1}, shown in Table 2. In the stacked CO[1–0] spectrum, we find a 3σ upper limit of <20 mJy km s^{-1}. In both cases, we have scaled the errors on the spectra using the prescription that $\mathtt{Var}(S_\nu/\sigma_\nu) = 1$ (where S_ν and σ_ν are the flux and associated error respectively in each line-free channel), thereby ensuring that they represent a true Gaussian distribution and are not underestimated. At the mean redshift of our targets, this corresponds to an upper

Downloaded from https://academic.oup.com/mnras/article/485/2/2092/5315777 by guest on 13 May 2022

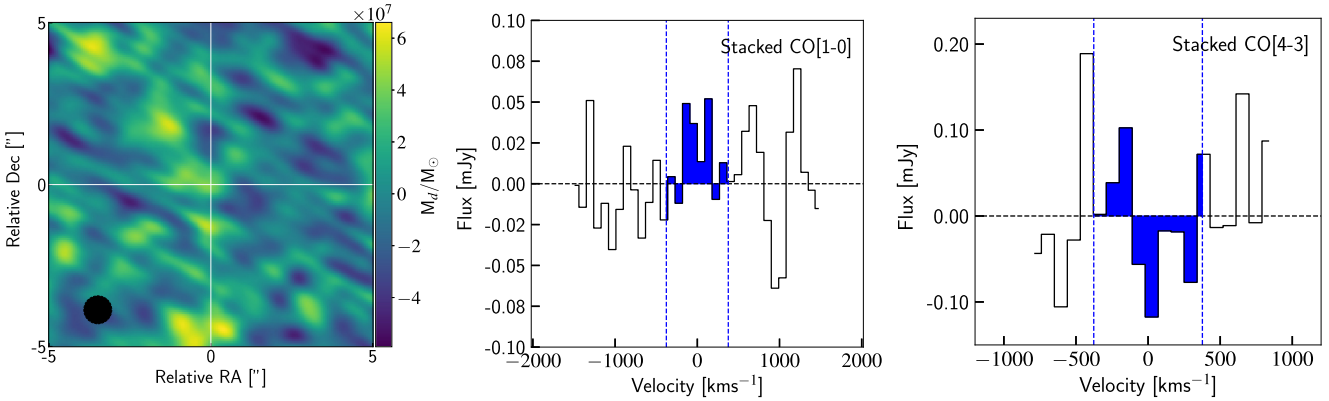


Figure 3. Left: stacked dust mass image for the five galaxies, created by combining the dust mass images from the 2 mm data and 870 μm data, as described in the text. The image is centred on the position of the stacked galaxies, and the white crosshair highlights the position of the peak pixel, used to derive the upper limit on dust mass. The average of the circularized beams for the two continuum datasets is shown in the bottom left corner. Centre: weighted-average stacked CO[1–0] spectrum of the five galaxies, binned into 90 km s^{-1} channels and shown against velocity relative to the expected position of the CO[1–0] line. The blue shading illustrates the average linewidth (containing 90 per cent of the flux) of the galaxies, $W_{90\%} = 753 \pm 22$ kms^{-1}, over which the stacked measurement was taken. Right: as for the centre panel, but for the CO[4–3] spectral stack. The CO[4–3] spectrum covers a smaller velocity range than the CO[1–0] stack, as the spectral resolution was coarser in the sidebands used for continuum measurements.

Table 3. ISM properties of individual galaxies in our sample, and of a stack of all five objects. $\log_{10}(M_{\rm mol}, {\rm KS})$ is the molecular gas mass inferred from $\rm SFR_{H\alpha}$ via the integrated Kennicutt–Schmidt relation for main-sequence galaxies (Sargent et al. 2014). CO[1–0] line luminosities, derived $\alpha_{\rm CO}$ conversion factors, dust masses, total G/D ratios, Hα linewidths from V15 and the expected CO 90 per cent flux widths ($W_{90\%}$) derived from these Hα lines are also listed. Upper limits on dust mass include the systematic errors discussed in the text. All upper/lower limits are placed at 3σ.

ID	$\log_{10}(M_{\rm mol}, {\rm KS})$ $\log_{10}(M_\odot)$	$\log_{10}(L'_{\rm CO[1-0]})$ $\log_{10}({\rm K\,km\,s^{-1}\,pc^2})$	$\alpha_{\rm CO}$ $\rm M_\odot(K\,km\,s^{-1}\,pc^2)^{-1}$	$\log_{10}(M_{\rm d})$ $\log_{10}(M_\odot)$	G/D –	$\sigma_{\rm H\alpha}$ (km s^{-1})	$\rm W_{90\%}$ (kms^{-1})
V568	$10.50^{+0.08}_{-0.10}$	<9.88	>4.3	<8.26	>176	224 ± 14	734 ± 45
V580	$10.62^{+0.10}_{-0.13}$	<9.88	>5.5	<8.04	>375	202 ± 27	779 ± 29
V422	$11.03^{+0.08}_{-0.10}$	<10.19	>6.9	<8.76	>183	237 ± 9	663 ± 89
V510	$10.61^{+0.09}_{-0.11}$	<10.05	>3.6	<8.77	>69	233 ± 20	763 ± 66
V105	$9.84^{+0.16}_{-0.25}$	<9.78	>1.1	<7.98	>51	169 ± 40	554 ± 130
Sample Ave.	$10.61^{+0.14}_{-0.20}$	<9.58	>10.61	<7.92	>478	–	753 ± 22

limit $\log(L'_{\rm CO[1-0]})$ <9.58 (see Table 3). We discuss the potential implications of these low CO luminosities in Section 4.1.

3.3 Dust continuum emission

In order to estimate the dust mass of the cluster galaxies, we convert between submillimetre continuum flux and dust mass, $M_{\rm d}$. This can be done separately for both the 870 μm and 2 mm continuum fluxes. As we cannot constrain the temperature of the dust with these data, we assume the shape of the $z = 2$ IR-to-sub-mm MS SED from Magdis et al. (2012), the shape of which is consistent with the individual limits on our continuum fluxes. We then calculate dust mass using

$$M_{\rm d} = \frac{L_{\rm IR}}{125\langle U\rangle} \propto \frac{4\pi d_{\rm L}^2}{125\langle U\rangle} \times F_\lambda \qquad (1)$$

where $d_{\rm L}$ is the luminosity distance of the galaxy, F_λ is either the 870 μm or 2 mm flux density and $\langle U\rangle$ is the mean, dust-weighted intensity of the stellar radiation field. The proportionality reflects the variable bolometric correction used to convert from sub-mm flux to $L_{\rm IR}$ for a given template shape (determined by our assumed value of $\langle U\rangle = 22$, in accordance with the redshift-evolution of this parameter measured in Béthermin et al. 2015). 125 is the average scaling factor between $L_{\rm IR}/M_{\rm d}$ from Magdis et al. (2012). If the dust temperatures in our galaxies were warmer than the template, as observed locally in low-mass and low-metallicity dwarf galaxies (e.g. Walter et al. 2007), this would in turn decrease the derived dust mass, and increase the G/D ratios. As we do not constrain the temperature, we allow a systematic error of 0.15 dex for these dust masses (Draine & Li 2007). In this way, we first calculate separate dust mass estimates from the 870 μm and 2 mm measurements (for V105, V580, and V568). The final dust mass of each galaxy is then calculated by combining the two dust mass estimates, weighted according to their errors. Where appropriate, the upper limit on the dust mass is calculated from this weighted average and associated error. For V422 and V510, the dust mass comes only from the 2 mm measurements.

Similarly to the CO emission, we find no significant dust continuum detections for these galaxies individually. The constraints on these dust masses are given in Table 3. We therefore created a stacked dust map for the five low-metallicity galaxies. To do this, we first made individual dust mass maps for each galaxy. We created 10 arcsec × 10 arcsec cut-outs centred on each galaxy, in both the 870μm and 2 mm data. This was done using the dirty image maps, having removed all other sources and corresponding sidelobes by simultaneous flux modelling of the entire field in GALFIT, using the full known dirty beam pattern. Each flux emission map (2 mm or 870 μm) was then converted to a dust mass map, pixel by pixel, for each galaxy, by converting between flux and dust mass as described

Downloaded from https://academic.oup.com/mnras/article/485/2/2092/5315777 by guest on 13 May 2022

above. All of these individual dust maps were then stacked in the image plane, by performing a weighted co-add of the images at each pixel position. The weights were determined by the primary beam corrected RMS noise in the individual image cut-outs. The stacked dust map is shown in Fig. 3.

As this image combines two datasets imaged with different synthesized beam shapes, PSF-fitting with GALFIT was not practical. If – as motivated in Section 2.2 based on their small optical sizes – the galaxies in the stack are unresolved, we can measure the dust mass associated with the stack by reading off the value of the central pixel in the stacked image and interpreting it as a peak flux measurement. We note that, as the circularized FWHM of the synthesized beams differ by only ~ 10 per cent, the two datasets sample similar spatial scales and have been imaged with the same pixel size. We find a 3σ upper limit on the stacked dust mass of $M_{\rm d} < 7.4 \times 10^7$ M$_\odot$. This small amount of dust seems consistent with initial expectations for low-metallicity galaxies, and we discuss how the dust and gas in these galaxies scale with metallicity in Section 4.2.2.

3.4 Molecular gas masses

We have calculated the molecular gas content of the galaxies by taking the Hα SFR of each galaxy, and using the integrated Kennicutt–Schmidt (KS, equation 5 of Sargent et al. 2014) law to convert between SFR and molecular gas mass $M_{\rm mol}$ as below:

$$M_{\rm mol} = {\rm SFR} \times \frac{1}{\rm SFE}. \quad (2)$$

As we do not know the star formation efficiencies (SFEs) of the galaxies, we assume that SFE increases smoothly with distance above the MS (e.g. Sargent et al. 2014; Tacconi et al. 2018), for each individual galaxy, to obtain molecular gas masses from SFR$_{\rm H\alpha}$. The assumption of these SFEs (corresponding to gas depletion times between $\sim$0.6 and 1.1 Gyr for our galaxies, with a sample median of 0.8 Gyr) is motivated by the position of our targets relative to the MS of star formation, and the consistency between the UV and Hα SFRs discussed below. We have no evidence that the galaxies have significantly increased SFEs or high gas excitation ratios. However, we also indicate the effect of a strongly increased SFE in Fig. 5. The molecular gas masses derived assuming an MS SFE are shown in Table 3. It is these gas masses that are used in the remainder of the analysis.

4 THE IMPACT OF A LOW GAS-PHASE METALLICITY ON ISM SCALING RELATIONS AT $z \sim 2$

A key outcome of this study is the notable lack of gas and dust detections in our star-forming galaxies. If we take the Hα SFRs of our galaxies, we would expect to detect the CO[4–3] and CO[1–0] emission at $\geq 3\sigma$ from 4/5 of our galaxies, assuming that the galaxies had BzK-like spectral line energy distributions (SLEDs, where BzK galaxies represent the 'normal', solar-enrichment population at this redshift). In the continuum data, we would expect to detect 3/5 of our galaxies at $\geq 3\sigma$ in the 2mm data (assuming a BzK-like SED), and to detect 2/3 of the galaxies covered by the 870 μm mosaic. However, we see in Section 3 that we do not detect any of our galaxies in these datasets. We now discuss the implications of these low detection fractions.

4.1 SFR–$L'_{\rm CO}$ correlations for $z = 2$, low-metallicity galaxies

Fig. 4(a) shows the relation between SFR and $L'_{\rm CO[1-0]}$ for galaxies in our sample, together with literature data compiled by Sargent et al. (2014) and containing MS galaxies at $0 < z < 3$. With the exception of V105, we see that the 3σ $L'_{\rm CO[1-0]}$ limits for our galaxies lie on, or to the left of, the reference trend from Sargent et al. (2014). The stacked $L'_{\rm CO[1-0]}$ limit is offset by $\sim$0.5 dex from this relation. This suggests that on average the galaxies have high SFRs given their $L'_{\rm CO[1-0]}$, and the stacked limit occupies the same part of parameter space as high-SFE starburst galaxies. However, the δMS values given in Table 1 indicate that our galaxies do not lie in the starburst regime in terms of their specific SFRs, with the exception of V422. An interpretation of this offset is then that the lack of $L'_{\rm CO[1-0]}$ in the galaxies is driven by their low gas-phase metallicities, consistent with an increased amount of photodissociation of CO molecules in diffuse clouds.

We also show in Fig. 4(a) the predicted locus of 'typical' $z \sim 0$ and $z \sim 2$ galaxies in SFR–$L'_{\rm CO[1-0]}$ space. To trace this locus we start from the log-linear integrated Kennicutt–Schmidt relation – expressed in terms of SFR and $M_{\rm H2}$ – from Sargent et al. (2014). We then associate to a given SFR and $M_{\rm H2}$ a metallicity-dependent CO-to-H2 conversion factor $\alpha_{\rm CO}$ via the following three steps. We assume that SFR and $M_\star$ are linked via the main-sequence relation, and $M_\star$ and metallicity via the MZR. We then consider $\alpha_{\rm CO}$ versus metallicity trends with a power-law form Z^γ, where $-2 < \gamma < -1$ (e.g. Israel 1997; Glover & Mac Low 2011; Leroy et al. 2011; Narayanan et al. 2012; Schruba et al. 2012; Amorín et al. 2016), as well as the prescription from Wolfire et al. (2010) (see also our Fig. 5a). We have normalized the relationship between $\alpha_{\rm CO}$ and metallicity so that a galaxy with the stellar mass of the Milky Way ($M_\star = 5.7 \times 10^{10}$ M$_\odot$, Licquia & Newman 2015) has $\alpha_{\rm CO} = 4.0$.[3] The expected SFR–$L'_{\rm CO[1-0]}$ relation starts to curve away from a simple log-linear trend at low $L'_{\rm CO[1-0]}$, with a 'detachment point' that shifts to higher luminosities with increasing redshift. While V422 and V580 are offset from the log-linear SFR–$L'_{\rm CO[1-0]}$ relation given by Sargent et al. (2014), the individual and stacked $L'_{\rm CO[1-0]}$ limits are more closely consistent with the expected locus for $z \sim 2$ galaxies. It should be noted here that the placement of starburst galaxies on this plane, offset from the SFR–$L'_{\rm CO[1-0]}$ relation, is driven by a high SFE compared with MS galaxies, rather than by low metallicity. The oxygen abundances of such high-z starbursts are typically higher than the galaxies discussed in this paper, consistent with solar metallicity (e.g. Rigopoulou et al. 2018).

For further evidence that a CO-deficit rather than an SFE-enhancement is responsible for the position of our low-metallicity galaxies in SFR–$L'_{\rm CO}$ space, we can also look at the SFR–$L'_{\rm CO[5-4]}$ plane shown in Fig. 4(b). $L'_{\rm CO[5-4]}$ was derived from the CO[4–3] data, assuming an MS, BzK-like excitation ($I_{\rm CO[5-4]} = 1.04 \times I_{\rm CO[4-3]}$, Daddi et al. 2015). The assumption of a BzK- or starburst-like excitation between CO[4–3] and CO[5–4] does not significantly affect the derivation of this quantity. The comparison dataset in this figure comprises local ULIRGs and spirals (Liu et al. 2015), BzK galaxies at $z \sim 1.5$ (Daddi et al. 2015) and high-z SMGs (Carilli & Walter 2013). The individual limits on our galaxies again lie to the left of the literature relations, and the stacked $L'_{\rm CO[5-4]}$ constraint lies at $\sim$0.5–0.7 dex below the $L'_{\rm CO[5-4]}$ that would be expected from a galaxy with this SFR. This

[3]We omit the units of $\alpha_{\rm CO}$ for brevity, but give $\alpha_{\rm CO}$ in units of M$_\odot$(K km s^{-1} pc^2)$^{-1}$ throughout this paper.

Downloaded from https://academic.oup.com/mnras/article/485/2/2092/5315777 by guest on 13 May 2022

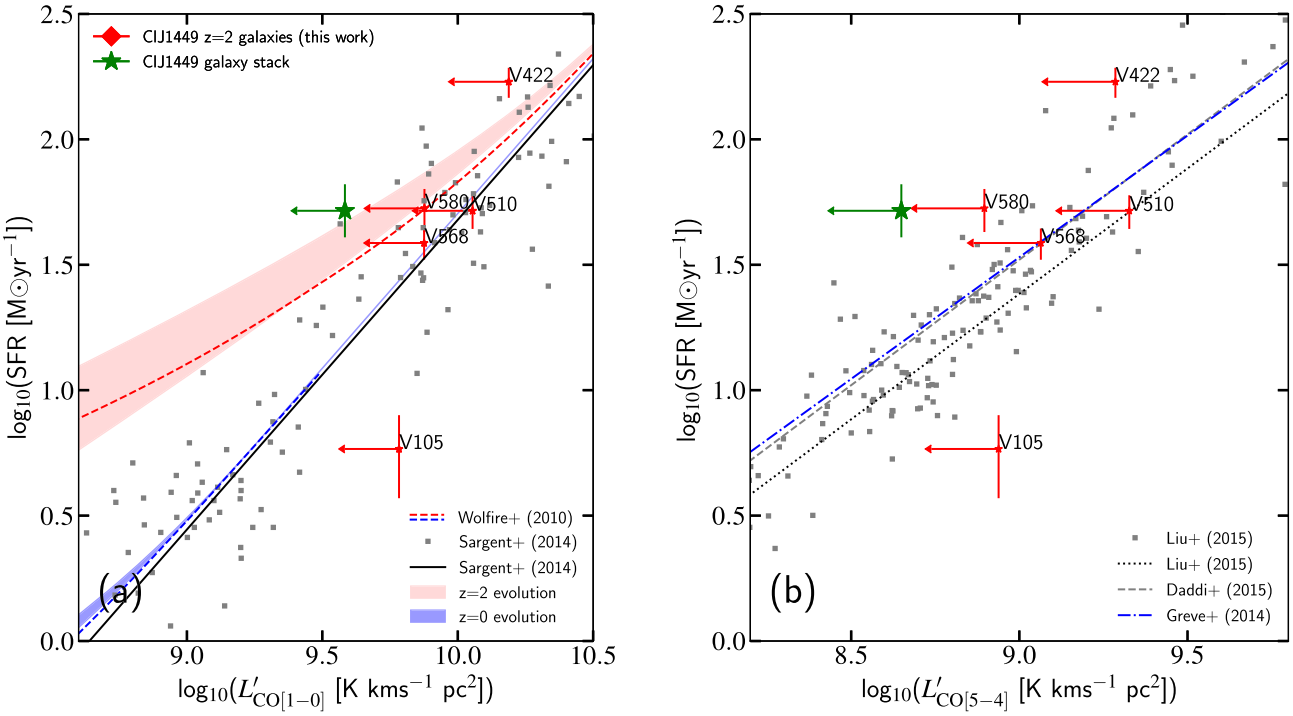


Figure 4. Left: $SFR_{H\alpha}$ versus $L'_{CO[1-0]}$, where upper limits are located at 3σ. Predicted evolutionary trends are shown for $z = 0.08$ and $z = 2$ by the blue- and red-shaded curves, assuming an α_{CO} versus metallicity slope between -1 (lower edge) and -2 (upper edge), as well as evolutionary trends predicted by Wolfire et al. (2010, dashed lines). Right: $SFR_{H\alpha}$ as a function of $L'_{CO[5-4]}$. The green stars show the stacked upper limit on $L'_{CO[1-0]}$ (left) and $L'_{CO[5-4]}$ (right, from the stacked CO[4–3] data), respectively. The vertical green error bar on the stack shows the formal error on the median Hα SFR. Previous literature relations are indicated in the legend. We see evidence for metallicity-driven, systematically decreased line emission from the diffuse, extended (traced by CO[1–0]) and denser molecular gas phases (traced by CO[5–4]) in our targets.

is particularly interesting, as Daddi et al. (2015) have shown that there is a tight, linear correlation between the CO[5-4] luminosity of a galaxy and its IR luminosity (and therefore SFR), regardless of whether the galaxy is MS or starbursting, with increased scatter only for the most extreme objects across cosmic time (Liu et al. 2015). The offset we see in Fig. 4(b) must therefore be a consequence of another physical property of the galaxies.

To test whether this offset could be due to an SFR time-scale effect, rather than low metallicity, we compare the Hα- and UV-SFRs in Table 1. Hα is a short time-scale (<10 Myr) tracer of star formation, whereas UV emission traces star formation on time-scales of ∼100 Myr (Calzetti 2008; Kennicutt & Evans 2012). The Hα- and UV-SFR estimates do not show large discrepancies, and are consistent to within $<2\sigma$, with the exception of very bright V422. The tension between these SFR indicators for V422 could indicate a recent increase in the SFR, but it should be noted that this comparison is dependent on the prescriptions of $E(B-V)$ used for continuum and nebular extinction. This indicates that the SFRs of the galaxies have remained fairly constant for the last 100 Myr, i.e. show no indication of a rapidly declining SFR (which in turn would lead to low CO[5–4] emission compared to the SFR–$L'_{CO[5-4]}$ trend, as CO[5–4] flux effectively represents an instantaneous SFR-tracer following Daddi et al. 2015). The clear offset of the stacked data in both panels of Fig. 4 is therefore unlikely to be driven by time-scale effects, and reinforces the conclusion that it is the low gas-phase metallicity in these galaxies that is driving the lack of CO emission at J = 1−0 and J = 4−3.

It is not clear to what extent one would expect the high-J transitions of CO to suffer the same effects of low enrichment as the low-J transitions. Studies of dwarf galaxies in the local Universe have revealed CO[3–2]/CO[1–0] and CO[2–1]/CO[1–0] line ratios consistent with those observed in local spiral galaxies (e.g. Sage et al. 1992; Meier et al. 2001; Cormier et al. 2014), indicating that photodissociation impacts the CO SLED up to at least the J = 3−2 transition in local low-metallicity galaxies. It is qualitatively understood that the effect of photodissociation is less prevalent in small regions of 'dense' CO gas (e.g. Bolatto et al. 2008), but it is not widely discussed to which CO excitation this extends to, and whether this is dependent on the individual galaxy. Aside from the destruction of CO by photodissociation, it is plausible that high-J excitation could be somewhat enhanced in low-metallicity environments, due to the stronger radiation field. We see in our galaxies that, despite this possibly enhancing effect, the molecular ISM at densities of $\sim 10^5$ cm^{-3} (∼40 × the critical density of the CO[1–0] molecule) nevertheless displays a significant CO-deficit, compared to the tight SFR–$L'_{CO[5-4]}$ relation observed for normal and starburst galaxies with approximately solar metallicity.

Although not well characterized to date, evidence that denser molecular gas phases in high-z galaxies can be affected by low metallicity has also been discussed by Tacconi et al. (2008) and Genzel et al. (2012), who find increasing numbers of galaxies at $z \sim 2$ (e.g. ZC406690, Mancini et al. 2011) that lack CO[3–2] emission compared to expectations. Our results suggest that this effect is present to even higher-J CO transitions at $z = 2$. We see evidence that the low metallicity in these galaxies may be either directly or indirectly influencing denser molecular gas reservoirs, implying that the linear correlation between CO[5-4] luminosity and SFR (which underpins SFR estimates based on CO emission)

Downloaded from https://academic.oup.com/mnras/article/485/2/2092/5315777 by guest on 13 May 2022

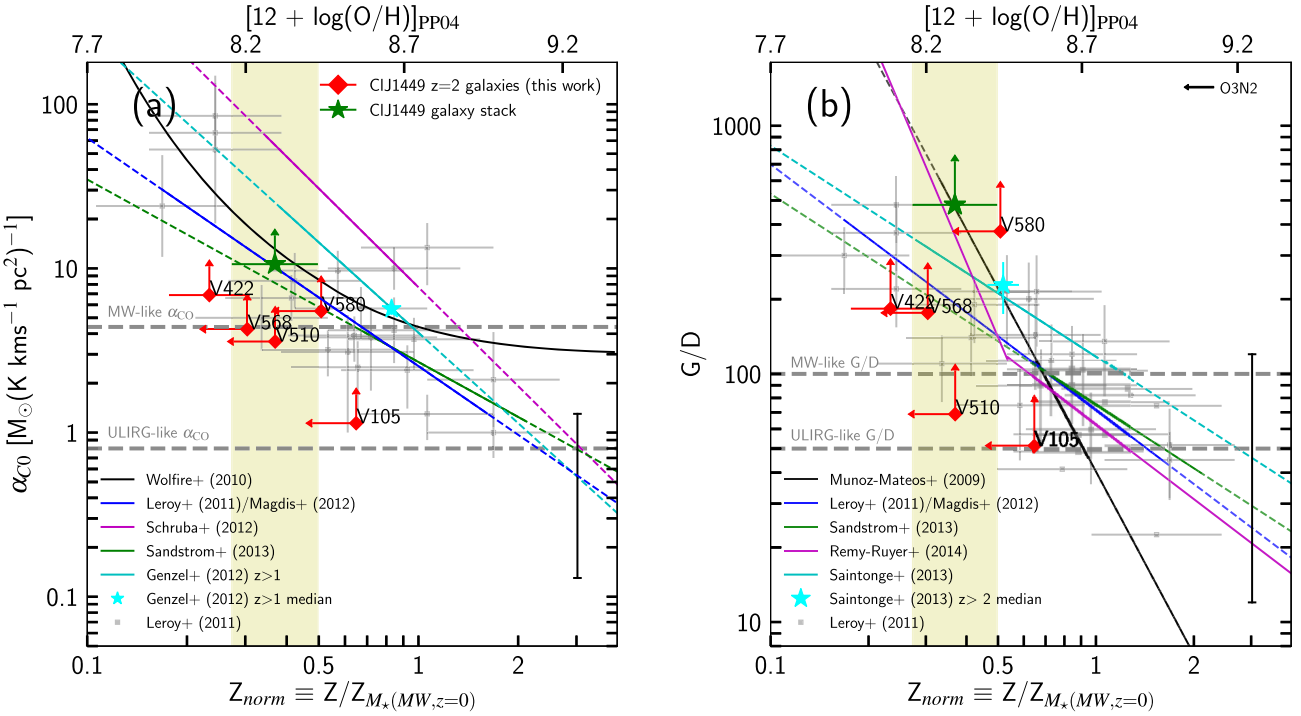


Figure 5. Left: CO-to-H_2 conversion factor α_{CO} as a function of metallicity. 3σ lower limits on α_{CO} are shown. Typical α_{CO} values for MW- and ULIRG-like galaxies are $\alpha_{CO} = 4.4$ and $\alpha_{CO} = 0.8$, respectively (Downes & Solomon 1998), shown by the grey dashed lines. Right: Gas-to-dust ratio as a function of metallicity. 3σ lower limits on the G/D ratio are shown. Typical G/D ratios of 100 and 50 for MW- and ULIRG-like galaxies respectively are indicated by the grey-dashed lines (Santini et al. 2014). In both panels, the comparison galaxy sample shown in grey comprises local galaxies, $z \sim 0.5$–2.5 galaxies, local ULIRGS and submillimetre galaxies, taken from Leroy et al. (2011) and Magdis et al. (2012). The upper x-axis gives the equivalent PP04 metallicity, valid for the individual galaxy data points reported in this figure. The horizontal black arrow in the top right corner of panel (b) indicates the median offset in metallicity that would result if the O3N2, rather than the N2 diagnostic were used. Previous literature trends are indicated in the legends, where for observational studies solid lines indicate the metallicity range sampled by the corresponding data (the dashed line segments illustrate the extrapolation of these trends to higher/lower metallicity). Each galaxy from our sample is shown by a red diamond. We show a representative error bar of 1 dex in the lower right corner, to illustrate by how much the quantity on the y-axis would decrease if the SFE was 10× higher, i.e. gas masses 10× lower. The stacked limit for the five galaxies is shown as a green star. The yellow-shaded region shows the error on the mean (stacked) metallicity of the galaxies.

may not hold for low-metallicity galaxies at $z = 2$. The deficit of CO emission in these galaxies is particularly relevant when considering high-J CO emission as an instantaneous star formation tracer (e.g. Lu et al. 2014; Daddi et al. 2015; Liu et al. 2015; Yang et al. 2017).

4.2 Metallicity-dependence of α_{CO} and G/D for $z \sim 2$ galaxies

The dependence of α_{CO} and G/D on metallicity at $z \sim 0$ follows a strong inverse relation, observationally following a power-law Z^{γ} or broken power-law shape (e.g. Draine & Li 2007; Wolfire et al. 2010; Leroy et al. 2011; Rémy-Ruyer et al. 2014). However, as discussed extensively in the literature (e.g. Kewley & Ellison 2008), different metallicity calibrations lead to systematically different gas-phase metallicity derivations (by up to ∼0.6 dex). These offsets lead to different normalizations for G/D and α_{CO} versus metallicity trends being reported in the literature (see e.g. Sandstrom et al. 2013). For example, at a fixed oxygen abundance value and when assuming a power-law dependence on metallicity with exponent $\gamma = -1$, mean G/D ratios (and α_{CO} values) will differ by a factor 4.7 when using two of the metallicity scales with among the largest systematic offsets, namely the Pilyugin & Thuan (2005, PT05) and Kobulnicky & Kewley (2004, KK04) systems, respectively. If we assume an even steeper slope with $\gamma = -2$, this discrepancy reaches a factor of 22 between the conversion factors derived using the PT05 and KK04 calibrations. It is therefore imperative to correct for the offsets between metallicity scales to ensure meaningful results and comparisons, as these systematics complicate making robust statements about the evolution of scaling relations with redshift.

For this reason, in the following we consider a normalized metallicity scale (see Fig. 5) which minimizes the systematic uncertainties introduced by different metallicity scales. We normalize all metallicities by the metallicity $Z_{M_\star(MW,z=0)}$ of a $z \sim 0$ Milky-Way-like galaxy of stellar mass $M_\star = 5.7 \times 10^{10}\,M_\odot$ (Licquia & Newman 2015), using the relevant local MZR for each calibration (Kewley & Ellison 2008). This is preferable to using a single, constant reference metallicity value, which has conflicting interpretations between different metallicity scales. For example, the canonical solar oxygen abundance $12 + \log_{10}(O/H)_\odot = 8.69$ (Asplund et al. 2009) is ∼0.3 dex higher than the typical MW-like metallicity of $Z = 8.37$ in the PT05 scale. Conversely, on the KK04 scale, the solar abundance value is ∼0.3 dex smaller than that of an MW-like galaxy. The advantage of our normalization approach is thus that we can reconcile scaling relations expressed in different metallicity calibrations by means of our calibration-dependent normalization factor $Z_{M_\star(MW,z=0)}$. If we were to instead convert the range of literature studies to one chosen metallicity system, we would find that straight-line, log-linear scaling relations in one system would map into curved loci in another. Converting to a normalized metallicity scale, as we have done, therefore preserves the shapes of the trend lines, and illustrates the full range of

Downloaded from https://academic.oup.com/mnras/article/485/2/2092/5315777 by guest on 13 May 2022

slopes reported in the literature. Additionally, conversions between certain metallicity calibrations are not available in Kewley & Ellison (2008), which would limit the relations available for comparison in this framework. Common calibrations used among literature relations are PT05, PP04, D02, and KK04, for which $Z_{M_*(MW,z=0)}$ equals 8.37, 8.77, 8.85, and 9.05 respectively as outlined above.

4.2.1 α_{CO} as a function of metallicity

Gas-phase metallicity is observed in the local Universe to have a direct effect on the α_{CO} conversion factors of low-metallicity galaxies (e.g. Leroy et al. 2007; Amorín et al. 2016; Accurso et al. 2017; Hunt et al. 2017). The low gas-phase metallicity strongly increases α_{CO}, as the lower metal content of the ISM leads to lower dust shielding of the CO molecule, which can consequently be photodissociated by UV radiation from young stars. This leads to 'CO-dark' H_2 gas.

Fig. 5(a) shows α_{CO} as a function of metallicity. For all galaxies in our sample we have placed lower limits on α_{CO} using the gas masses inferred in Section 3.4 and the upper limits on the CO[1–0] luminosities listed in Table 3:

$$\alpha_{CO} = \frac{M_{mol}}{L'_{CO[1-0]}} = \frac{SFR}{SFE}\frac{1}{L'_{CO[1-0]}}. \quad (3)$$

We plot in Fig. 5(a) the relations observed by Genzel et al. (2012), Magdis et al. (2012), Schruba et al. (2012), and Sandstrom et al. (2013), and model predictions from Wolfire et al. (2010). The Genzel et al. (2012) sample comprises MS galaxies at $z > 1$, and Magdis et al. (2012) fit local MS spiral galaxies from Leroy et al. (2011) with MS galaxies at $0.5 < z < 1.5$. Schruba et al. (2012) use observations of HERACLES local dwarf galaxies to derive the relation shown, and Sandstrom et al. (2013) study local HERACLES star-forming galaxies, the majority of which (25/26) are spiral galaxies.

The 3σ lower limits on α_{CO} shown for our sample in Fig. 5(a) are consistent with the measured trends at low metallicity in the local Universe (e.g. Leroy et al. 2011; Schruba et al. 2012; Sandstrom et al. 2013). Our deeper constraint on α_{CO} from stacking (green star in Fig. 5a) is also consistent with these low-z trends, as well as the model predictions from Wolfire et al. (2010).

We also show the result of a study at higher redshift, conducted by Genzel et al. (2012). Genzel et al. (2012) studied the effect of metallicity on α_{CO} including MS galaxies up to $z \sim 2$, tracing the molecular gas through the CO[3–2] and CO[2–1] transitions. In order to calculate these conversion factors, Genzel et al. (2012) take a near-unity KS slope of $n = 1.1$. The inclusion of our data extends this work, allowing us to study this trend down to a lower median metallicity than the Genzel et al. (2012) sample, directly using the ground-state transition CO[1–0]. We find that both our individual and stacked limits are consistent with the $z > 1$ Genzel et al. (2012) trend. We perform a linear fit between the median α_{CO} and metallicity of the $z > 1$ galaxies analysed by Genzel et al. (2012) (cyan star in Fig. 5a) and our stacked limit. We find a lower limit on the dependence with metallicity of $Z^{-0.8}$, which is shallower than the low-redshift studies presented in Fig. 5(a), but consistent with the range of slopes present in the literature (e.g. Wilson 1995; Arimoto, Sofue & Tsujimoto 1996; Bolatto et al. 2008). This value does not suggest a steeper slope between α_{CO} and metallicity at high redshift than in the local Universe, as Genzel et al. (2012) report, but it is based on limited statistics and a low-S/N CO[1–0] flux constraint. It should also be noted that the Genzel et al. (2012) sample contains a larger number of galaxies in the range $1 \leq z \leq 1.5$ than at $2 \leq z \leq 2.4$, and therefore has a lower median redshift than our stacked sample.

To summarize, Fig. 5(a) demonstrates that low-enrichment galaxies at $z = 2$ have higher α_{CO} values than their more enriched counterparts, consistent with what is found in the local Universe. We now look at the G/D ratios of these galaxies, to explore the impact of low metallicity at high redshift when deriving gas masses from dust continuum emission.

4.2.2 Gas-to-dust ratio as a function of metallicity

As ISM spectroscopy of galaxies is time-consuming and not always feasible, approaches to using the dust continuum emission of galaxies to estimate gas mass have also been developed (e.g. Guelin et al. 1993; Corbelli et al. 2012; Eales et al. 2012; Magdis et al. 2012; Bourne et al. 2013; Scoville et al. 2014; Groves et al. 2015). A typical value for the G/D ratio of a 'normal', solar-metallicity galaxy in the local Universe is ∼100 (Draine & Li 2007). We show the G/D ratio as a function of metallicity in Fig. 5(b). We have calculated the dust masses of the galaxies using their continuum emission at 2mm and 870 μm where possible, as discussed in Section 3.3. The G/D ratio is calculated as below, where the gas mass derivation is described in Section 3.4:

$$G/D = \frac{M_{mol} + M_{HI}}{M_d} \simeq \frac{M_{mol}}{M_d} = \frac{SFR}{SFE}\frac{1}{M_d}. \quad (4)$$

We assume, following standard practice, that the gas phase in our galaxies at $z = 2$ is dominated by molecular gas (Daddi et al. 2010b; Genzel et al. 2015; Lagos et al. 2015; Tacconi et al. 2018). In addition to the individual G/D ratios, we show in Fig. 5(b) the stacked limit on the G/D ratio. It should be noted that Fig. 5(b) shows total gas to dust ratios. In the case of local galaxies, where the molecular gas is not necessarily dominant, the total gas mass therefore also includes atomic hydrogen. The contribution of elements heavier than hydrogen is also accounted for at all redshifts.[4]

We can use Fig. 5(b) to evaluate whether low-metallicity galaxies at $z = 2$ follow the same scaling relation between G/D and metallicity as local galaxies (e.g. Sandstrom et al. 2013; Rémy-Ruyer et al. 2014), and compare our sample with the high-z study from Saintonge et al. (2013). Magdis et al. (2012) and Sandstrom et al. (2013) use the same galaxy samples described in Section 4.2.1. Muñoz-Mateos et al. (2009) use observations from the local SINGS galaxy sample, and Rémy-Ruyer et al. (2014) also study local galaxies, including dwarf galaxies from the Dwarf Galaxy Survey and KINGFISH. Saintonge et al. (2013) use observations of ∼7 lensed normal star-forming galaxies at $z \sim 2$. The best-fitting relations derived from each of these works are shown in Fig. 5(b).

With the exception of Muñoz-Mateos et al. (2009), the scaling relations from the literature display an approximately linear decrease of the G/D ratio with metallicity above $\sim 0.5 Z_{norm}$. Below $\sim 0.5 Z_{norm}$, a split occurs, where Magdis et al. (2012), Saintonge et al. (2013), and Sandstrom et al. (2013) predict a shallower

[4]We note that the prescriptions of Galliano et al. (2011), adopted by Rémy-Ruyer et al. (2014) to derive dust masses, and the one used by Sandstrom et al. (2013) and in our work (Draine & Li 2007) are different. As Sandstrom et al. (2013) and Rémy-Ruyer et al. (2014) derive G/D ratios for a number of the same KINGFISH galaxies, we renormalize the G/D ratios in Rémy-Ruyer et al. (2014) by the mean G/D of the Sandstrom et al. (2013) sample, G/D = 92.

Downloaded from https://academic.oup.com/mnras/article/485/2/2092/5315777 by guest on 13 May 2022

dependence of G/D on Z than Muñoz-Mateos et al. (2009) and Rémy-Ruyer et al. (2014). Our stacked sample in particular probes this lower metallicity regime at $z = 2$.

We find that the individual G/D ratios of our low-metallicity galaxies are consistent with all of the local relations shown (noting that all galaxies except V422 are also 2σ upper limits on metallicity), as well as the $z > 2$ relation from Saintonge et al. (2013). Saintonge et al. (2013) report an increased normalization at $z > 2$ of a factor 1.7 compared with the local Leroy et al. (2011) relation. We show the median metallicity and G/D from Saintonge et al. (2013) in Fig. 5(b), and find the difference between this value and the Leroy et al. (2011) relation to remain consistent with this factor 1.7 increase also after scaling of all studies to a common, renormalized metallicity scale. We do however note that the local relation of Muñoz-Mateos et al. (2009) shown in Fig. 5(b) is also consistent with the Saintonge et al. (2013) median data point at $z > 2$.

When we consider our stacked G/D limit, we see a clear elevation above the relations presented by Magdis et al. (2012), Saintonge et al. (2013) and Sandstrom et al. (2013) at this metallicity. We verify through jackknife analysis that this stacked G/D ratio is not strongly driven by the G/D of V580. We strongly favour the case of an increased G/D ratio at significantly sub-solar metallicities, as seen in our sample. Our stacked limit is in good agreement with both the relations of Muñoz-Mateos et al. (2009) and Rémy-Ruyer et al. (2014) at this metallicity. Note also that Rémy-Ruyer et al. (2014) would derive higher G/D ratios if they were to assume MW-like dust grains, as discussed in Galliano et al. (2011), giving a steeper slope between G/D and metallicity. Fig. 5(b) suggests that our galaxies at $z = 2$ would be consistent with the Rémy-Ruyer et al. (2014) relation even for the steeper slope resulting as a consequence of adopting MW-like dust grains. We find a lower limit on the slope between our stacked G/D limit and the median Saintonge et al. (2013) value of -2.2, compared with the slopes of -2.45 and -3.10 found by Muñoz-Mateos et al. (2009) and Rémy-Ruyer et al. (2014) in this metallicity regime, respectively. The calculation of gas masses in our galaxies accounts for the increase in SFE for galaxies above the MS. In order for the lower limit on our G/D versus Z slope to become consistent with the slope of local relations from Magdis et al. (2012) and Sandstrom et al. (2013), the average SFE would need to increase by at least an additional factor of 1.5. The depletion time-scale fit given by Tacconi et al. (2018), which suggests a steeper evolution of SFE with offset from the MS than Sargent et al. (2014), as well as a dependence of SFE on stellar mass, is consistent with this order of decrease in G/D limit.

The constraints provided by our data are compatible with a G/D−metallicity relation at $z \sim 2$ that does not evolve compared to low redshift. However, they strongly support a steep dependence on metallicity at low enrichment, as shown by Rémy-Ruyer et al. (2014). They are also in agreement with the fudicial model predictions of Popping, Somerville & Galametz (2017), which reproduces the double power-law shape observed by Rémy-Ruyer et al. (2014), and predicts only weak evolution of the G/D ratio with redshift (<0.3 dex increase in G/D at $<0.5\,Z_{\odot}$ from $z = 0$ to $z = 9$).

It is not trivial to assess how deviations of our galaxies from the star-forming MS (1.6σ above, on average) affect the position of these galaxies on scaling relations of G/D and α_{CO} versus metallicity (Sections 4.2.1 and 4.2.2). It has been established that galaxies above the MS tend to have larger gas fractions that those galaxies below the MS (e.g. Magdis et al. 2012; Saintonge et al. 2012; Santini et al. 2014; Sargent et al. 2014; Scoville et al. 2017; Tacconi et al. 2018). However, gas-phase metallicity may also correlate with offset from the MS (as given by the fundamental metallicity relation, FMR, Lara-López et al. 2010; Mannucci et al. 2010), where an increase in SFR at fixed stellar mass implies lower gas-phase metallicity (see e.g. Sanders et al. 2015, Onodera et al. 2016 and Cresci, Mannucci & Curti 2018 for discussion on the existence of an FMR beyond the local Universe). Selection of galaxies with a systematic offset with respect to the MS may therefore not necessarily lead to shifts above and below the scaling relations we present here, but certainly have a component along the metallicity axis of these relations. However, the effect of main-sequence offset on ISM scaling relations cannot be dissected with the number of galaxies studied in this paper.

4.3 Implications for gas mass derivations at $z \sim 2$

Figs 5(a) and (b) demonstrate that the sub-solar metallicity of our galaxies at $z = 2$ is impacting both the CO-to-H_2 conversion factor α_{CO} and G/D ratio of the galaxies in our sample. Here we explore the implications of this for molecular gas mass calculations in the sub-M^* mass regime at the peak epoch of star formation.

4.3.1 Gas content of individual sub-M^* galaxies

As discussed, the most simplistic approach to measuring gas masses is to assume that α_{CO} or G/D does not vary with metallicity. In this case, MW-like conversion factors are often assumed regardless of a galaxy's properties. We find that our stacked α_{CO} limit lies a factor >2.4 above the MW value $\alpha_{CO} = 4.4$. The deviation from a constant MW value will continue to increase at lower enrichment. Similarly, if we take a constant MW G/D = 100, the G/D of our stack implies gas masses >4.8 times higher than would be inferred from the MW value.

Another approach one might take to calculate gas masses is to use conversion factors based on a well-studied population of galaxies at a given redshift (e.g. for $z \sim 2$, galaxies with stellar masses $10^{10}-10^{11}\,M_{\odot}$). However, galaxies at the knee of the stellar mass function ($M_{\star} \sim 10^{10.4}\,M_{\odot}$; e.g. Davidzon et al. 2017) at $z \sim 2$ have metallicities approximately ∼0.47 dex higher than, e.g. $M_{\star} \sim 10^{9}\,M_{\odot}$ galaxies, depending on the metallicity calibration used (Kewley & Ellison 2008; Zahid et al. 2014). Taking a slope of $\log_{10}(\alpha_{CO})$ versus metallicity of -0.8 as suggested by our data would therefore give rise to an underestimation of the gas mass from CO by at least a factor 3, remembering that our data give a lower limit on this slope. Additionally, there is a steep dependence of G/D on metallicity in this regime ($<0.5Z_{M_{\star}(MW,z=0)}$), where $\mathrm{G/D} \propto Z^{-2.2}$ or even steeper according to our data. We see in Fig. 5(b) that applying the G/D ratio of an $M_{\star} \sim 10^{10.4}\,M_{\odot}$ galaxy to an $M_{\star} \sim 10^{9}\,M_{\odot}$ galaxy at $z = 2$ would result in an underestimation of the gas mass by a factor >17 (Zahid et al. 2014).

These calculations highlight the importance of using physically motivated conversion factors when deriving gas masses for low enrichment or sub-M^* galaxies. Assuming MW-like conversion factors or factors appropriate for more massive galaxies would result in an underestimation of the molecular gas mass from both continuum and line emission.

4.3.2 Which galaxy population dominates the cosmic gas density at $z \sim 2$?

Finally, it is interesting to consider the implications of these findings for measurements of the cold gas history of the universe (e.g. Lagos et al. 2011; Popping, Somerville & Trager 2014; Walter et al. 2014;

Downloaded from https://academic.oup.com/mnras/article/485/2/2092/5315777 by guest on 13 May 2022

Decarli et al. 2016; Scoville et al. 2017; Riechers et al. 2019), and in particular for the determination of which characteristic stellar mass scale contributes most to the comoving molecular gas density. Whether – given a set of observed dust masses or molecular line luminosities – we infer this to be, e.g. the M* population or galaxies at lower masses partially depends on how strongly α_{CO} and G/D ratios depend on metallicity. The contribution of galaxies with stellar mass $M_\star$ to the comoving molecular gas density is

$$\rho_{H_2}(M_\star) \propto \Phi(M_\star)\langle M_{H_2}\rangle_{M_\star} \propto \Phi(M_\star)\langle\alpha_{CO}L'_{CO[1-0]}\rangle_{M_\star} \quad (5)$$

(or $\rho_{H_2}(M_\star) \propto \Phi(M_\star)\langle G/D \times M_d\rangle_{M_\star}$). Here $\langle M_{H_2}\rangle_{M_\star}$ is the characteristic H_2 mass of galaxies with stellar mass $M_\star$, and $\Phi(M_\star)$ is the comoving number density of galaxies with a given stellar mass, e.g. from the stellar mass function of actively star-forming galaxies in Davidzon et al. (2017). For $\log_{10}(M_\star) = 9$ (10.4) at $z \sim 2$, $\log_{10}(\Phi(M_\star)) = -2.26$ (-2.86), corresponding to a four-fold higher number density of $M_\star \sim 10^9$ M$_\odot$ systems, but a ∼6-fold higher contribution of $10^{10.4}$ M$_\odot$ galaxies to the comoving stellar mass density $\rho(M_\star)$. By how much will the larger α_{CO} values for sub-M^* galaxies modify the relative contribution of these two stellar mass bins in terms of the $z \sim 2$ cosmic gas mass density (compared to their contribution to the stellar mass density)?

Using our derived lower limits on the slopes of the $\log_{10}(\alpha_{CO})$ and $\log_{10}$(G/D) versus Z relations, we can derive a lower bound on the relative contribution to the cosmic gas mass density of galaxies at $M_\star = 10^9$ M$_\odot$M$_\odot$, and at the knee of the stellar mass function at $M^* = 10^{10.4}$ M$_\odot$. We find an increased ratio $\frac{\rho_{H_2}(M_\star=10^9\,M_\odot)}{\rho_{H_2}(M_\star=10^{10.4}\,M_\odot)} > 11 \times \frac{L'_{CO[1-0]}(M_\star=10^9\,M_\odot)}{L'_{CO[1-0]}(M_\star=10^{10.4}\,M_\odot)}$ of the comoving gas densities when using a metallicity dependent α_{CO}, compared with the considerably smaller increase of four times the $L'_{CO[1-0]}$ ratio when a constant MW-like α_{CO} is assumed. When a metallicity dependent G/D is used, we find an increase in the comoving gas density of $\frac{\rho_{H_2}(M_\star=10^9\,M_\odot)}{\rho_{H_2}(M_\star=10^{10.4}\,M_\odot)} > 68 \times \frac{M_d(M_\star=10^9\,M_\odot)}{M_d(M_\star=10^{10.4}\,M_\odot)}$, compared to just four times the dust mass ratios when a constant G/D is assumed. For the contribution to the $z \sim 2$ cosmic gas mass density of sub-M^* galaxies, $\rho_{H_2}(M_\star = 10^9\,M_\odot)$, to become at least as large as that of galaxies at the knee of the stellar mass function, the ratio of the typical $L'_{CO[1-0]}$ (M_d) values in the low-mass bin over that in the high-mass bin would thus have to be ≥0.09 (≥0.015). If we follow the same formalism as in Section 4.1 to relate SFR, $M_\star$, M_{H_2}, and Z for average galaxies in these mass bins (namely using the star formation MS, the MZR, and the integrated KS law to find SFR, metallicity, and molecular gas mass, for a given $M_\star$), and take a power-law index $\gamma = -0.8$ of α_{CO} versus metallicity from our data to derive α_{CO}, we can estimate average $L'_{CO[1-0]}$ values for these stellar mass bins at $z = 2$ (using $L'_{CO[1-0]} = M_{mol}/\alpha_{CO}$). We predict the average $L'_{CO[1-0]}$ ratio to be 0.045, indicating that despite the increased α_{CO} in sub-M^* galaxies, the population at $M_\star = 10^9$ M$_\odot$ has not overtaken that at $M^* = 10^{10.4}$ M$_\odot$ in terms of their contributions to the comoving gas mass density at $z \sim 2$. This also implies a much lower CO detection rate for low-mass galaxies at $z = 2$, compared with more massive, enriched galaxies.

Rising CO-to-H_2 conversion factors and G/D ratios at low mass/metallicity do, however, significantly shift the balance between different galaxy mass scales compared to the stellar mass density distribution. For example, in our example involving a metallicity-dependent α_{CO}, a more than six-fold higher contribution of M^* galaxies to $\rho(M_\star)$ was reduced to an only 2× higher contribution to $\rho(M_{H_2})$, compared to the $M_\star = 10^9$ M$_\odot$ population.

5 CONCLUSIONS

This paper explores the relationship between molecular gas, dust, star formation, and metallicity in five sub-solar enrichment galaxies (average oxygen abundance ∼0.35 dex below solar) at $z \sim 2$. Studying the ISM of these sub-M^* galaxies gives us a greater understanding of how low-metallicity ISM scaling relations at $z = 2$ compare with those calibrated in the local Universe, and on more massive and luminous $z \sim 2$ galaxies. Limits on the oxygen abundance of these galaxies were first constrained by Valentino et al. (2015), making use of the galaxies' bright H α detections. Here we follow the same procedure to derive a sample average metallicity of $Z = 8.34 \pm 0.13$ (PP04 N2 calibration).

Using deep ALMA and VLA data, we search for the CO[1–0] and CO[4–3] lines and 870 μm and 2 mm continuum emission from our targets, but find that they remain individually undetected. These non-detections highlight the low ISM enrichment of our galaxies, particularly when comparing with the expected detection percentage (60–80 per cent) in our data, for solar enrichment galaxies with these H α SFRs. We perform stacked analysis on the CO spectra and dust emission in order to place more stringent limits on the average ISM content of the five galaxies, and once again find these quantities undetected in the stacked data.

We place our galaxies on the $L'_{CO[1-0]}$–SFR plane, and see that our sample average has an offset of >0.5 dex below the expected $L'_{CO[1-0]}$, occupying the same parameter space as high-SFE starburst galaxies. We verify that this offset is driven by neither a recent increase in star formation nor a high SFE in our galaxies. We therefore interpret this as evidence that the low metal enrichment of the ISM in our galaxies at $z = 2$ is leading to dissociation of CO in the diffuse ISM phase, as seen in the local Universe.

This CO deficit also manifests itself for the denser ISM phases which are traced by CO[4–3]. We convert our stacked CO[4–3] constraint to CO[5–4] luminosity using a BzK excitation correction, in order to examine the position of our galaxies on the $L'_{CO[5-4]}$–SFR plane. We find an average luminosity of >0.5–0.7 dex less than the expected CO[5–4] luminosity. The position of galaxies on this relation is invariant to their star formation efficiency, confirming that this CO deficit is most likely driven by the low gas-phase metallicity. This has important implications, as it could lead to systematic underestimation of the instantaneous SFRs of low-metallicity galaxies as traced through high-J CO transitions.

In order to investigate how the ISM properties of our galaxies scale with metallicity at $z = 2$, we calculate molecular gas masses using the H α SFRs, assuming an MS SFE. We then derive limits on the α_{CO} conversion factors and G/D ratios of the galaxies. We find a power-law slope of α_{CO} (G/D) versus metallicity at $z \sim 2$ of $\gamma < -0.8$ ($\gamma < -2.2$), consistent with dependencies observed at $z = 0$. We stress the importance of comparing studies using different metallicity calibrations on a normalized metallicity scale, and place a compilation of literature scaling relations alongside our data. When systematic differences in metallicity are taken into account in this way, we find consistency between both the α_{CO} and G/D versus metallicity relations at $z = 2$ compared with local relations. However, our stacked G/D limit strongly favours a steep G/D versus Z slope at low metallicity (∼$0.5Z_{M_\star(MW,z=0)}$), consistent with the double power-law relation given by Rémy-Ruyer et al. (2014).

Finally, we discuss the implications of these results on the calculation of molecular gas masses in low-metallicity, $z = 2$, galaxies. We find that the assumption of G/D and α_{CO} values based on the more routinely observed M^* population at this redshift (or

Downloaded from https://academic.oup.com/mnras/article/485/2/2092/5315777 by guest on 13 May 2022

uniform application of the 'canonical' MW-like conversion factors) would result in significant underestimation of the gas mass in these low-metallicity galaxies. We predict the average contribution of sub-M^* galaxies with $M_\star = 10^9\,\mathrm{M}_\odot$ to the comoving molecular gas density at $z = 2$, and find that their increased α_{CO} values are not sufficient for this population to become dominant over M^* galaxies in this respect. However, we see that increased α_{CO} and G/D conversion factors at low enrichment significantly shift the balance between different galaxy mass scales compared to their relative contribution to stellar mass density distributions.

Our analysis has enabled us to place observational constraints on the ISM properties of low-enrichment galaxies at the peak epoch of star formation. In combination with future, similar studies, this kind of work can inform the design of ISM surveys of sub-M^* galaxies. Going forward, collating larger, statistical samples of galaxies spanning a large metallicity range will allow us to determine, e.g. the influence of starburstiness or MS-offset on the scatter of the ISM scaling relations studied here. To our knowledge, this has not yet been quantified at low or high redshift. In this way we will continue to explore the effect of low gas-phase metallicity on the interstellar medium, and characterize the evolution of the ISM outside of the local Universe.

ACKNOWLEDGEMENTS

We thank the anonymous referee, whose comments improved the clarity and quality of this paper. RTC acknowledges support from the Science and Technology Facilities Council (grant ST/N504452/1) and the University of Sussex. MTS was supported by a Royal Society Leverhulme Trust Senior Research Fellowship (LT150041).

This paper makes use of the following ALMA data: ADS/JAO.ALMA#2012.1.00885.S and ADS/JAO.ALMA#2015.1.01355.S. ALMA is a partnership of ESO (representing its member states), NSF (USA) and NINS (Japan), together with NRC (Canada), MOST and ASIAA (Taiwan), and KASI (Republic of Korea), in cooperation with the Republic of Chile. The Joint ALMA Observatory is operated by ESO, AUI/NRAO, and NAOJ.

This paper also makes use of VLA program 12A-188. The National Radio Astronomy Observatory is a facility of the National Science Foundation operated under cooperative agreement by Associated Universities, Inc.

REFERENCES

Accurso G. et al., 2017, MNRAS, 470, 4750
Amorín R., Muñoz-Tuñón C., Aguerri J. A. L., Planesas P., 2016, A&A, 588, A23
Aravena M. et al., 2010, ApJ, 718, 177
Arimoto N., Sofue Y., Tsujimoto T., 1996, PASJ, 48, 275
Asplund M., Grevesse N., Sauval A. J., Scott P., 2009, ARA&A, 47, 481
Baldwin J. A., Phillips M. M., Terlevich R., 1981, PASP, 93, 5
Belfiore F. et al., 2015, MNRAS, 449, 867
Béthermin M. et al., 2015, A&A, 573, A113
Bolatto A. D., Leroy A. K., Rosolowsky E., Walter F., Blitz L., 2008, ApJ, 686, 948
Bourne N. et al., 2013, MNRAS, 436, 479
Burstein D., Heiles C., 1982, AJ, 87, 1165
Calzetti D., 2008, in Knapen J. H., Mahoney T. J., Vazdekis A., eds, ASP Conf. Ser. Vol. 390, Pathways Through an Eclectic Universe. Astron. Soc. Pac., San Francisco, p. 121
Calzetti D., Armus L., Bohlin R. C., Kinney A. L., Koornneef J., Storchi-Bergmann T., 2000, ApJ, 533, 682
Carilli C. L., Walter F., 2013, ARA&A, 51, 105
Chabrier G., 2003, PASP, 115, 763
Coogan R. T., et al., 2018, MNRAS, 479, 703
Corbelli E. et al., 2012, A&A, 542, A32
Cormier D. et al., 2014, A&A, 564, A121
Cresci G., Mannucci F., Curti M., 2018, preprint (arXiv:1811.06015)
Daddi E. et al., 2010a, ApJ, 713, 686
Daddi E. et al., 2010b, ApJ, 714, L118
Daddi E. et al., 2015, A&A, 577, A46
Davidzon I. et al., 2017, A&A, 605, A70
Decarli R. et al., 2016, ApJ, 833, 70
Denicoló G., Terlevich R., Terlevich E., 2002, MNRAS, 330, 69 (D02)
Downes D., Solomon P. M., 1998, ApJ, 507, 615
Draine B. T., Li A., 2007, ApJ, 657, 810
Draine B. T. et al., 2007, ApJ, 663, 866
Eales S. et al., 2012, ApJ, 761, 168
Erb D. K., Shapley A. E., Pettini M., Steidel C. C., Reddy N. A., Adelberger K. L., 2006, ApJ, 644, 813
Galliano F. et al., 2011, A&A, 536, A88
Genzel R. et al., 2010, MNRAS, 407, 2091
Genzel R. et al., 2012, ApJ, 746, 69
Genzel R. et al., 2015, ApJ, 800, 20
Glover S. C. O., Mac Low M.-M., 2011, MNRAS, 412, 337
Gobat R. et al., 2011, A&A, 526, A133
Gobat R. et al., 2013, ApJ, 776, 9
Grenier I. A., Casandjian J.-M., Terrier R., 2005, Science, 307, 1292
Groves B. A. et al., 2015, ApJ, 799, 96
Guelin M., Zylka R., Mezger P. G., Haslam C. G. T., Kreysa E., Lemke R., Sievers A. W., 1993, A&A, 279, L37
Hunt L. K. et al., 2017, AAP, 606, A99
Ilbert O. et al., 2010, ApJ, 709, 644
Ilbert O. et al., 2013, A&A, 556, A55
Israel F. P., 1997, A&A, 328, 471
Issa M. R., MacLaren I., Wolfendale A. W., 1990, A&A, 236, 237
Kashino D. et al., 2013, ApJ, 777, L8
Kennicutt R. C., Evans N. J., 2012, ARA&A, 50, 531
Kewley L. J., Dopita M. A., 2002, ApJS, 142, 35
Kewley L. J., Ellison S. L., 2008, ApJ, 681, 1183
Kewley L. J., Maier C., Yabe K., Ohta K., Akiyama M., Dopita M. A., Yuan T., 2013, ApJ, 774, L10
Kobulnicky H. A., Kewley L. J., 2004, ApJ, 617, 240 (KK04)
Kriek M., van Dokkum P. G., Labbé I., Franx M., Illingworth G. D., Marchesini D., Quadri R. F., 2009, ApJ, 700, 221
Lagos C. D. P., Baugh C. M., Lacey C. G., Benson A. J., Kim H.-S., Power C., 2011, MNRAS, 418, 1649
Lagos C. D. P. et al., 2015, MNRAS, 452, 3815
Lara-López M. A. et al., 2010, A&A, 521, L53
Leroy A., Cannon J., Walter F., Bolatto A., Weiss A., 2007, ApJ, 663, 990
Leroy A. K. et al., 2011, ApJ, 737, 12
Licquia T. C., Newman J. A., 2015, ApJ, 806, 96
Liu D., Gao Y., Isaak K., Daddi E., Yang C., Lu N., van der Werf P., 2015, ApJ, 810, L14
Lu N. et al., 2014, ApJ, 787, L23
Magdis G. E. et al., 2011, ApJ, 740, L15
Magdis G. E. et al., 2012, ApJ, 760, 6
Mancini C. et al., 2011, ApJ, 743, 86
Mannucci F., Cresci G., Maiolino R., Marconi A., Gnerucci A., 2010, MNRAS, 408, 2115
McMullin J. P., Waters B., Schiebel D., Young W., Golap K., 2007, in Shaw R. A., Hill F., Bell D. J., eds, ASP Conf. Ser. Vol. 376, Astronomical Data Analysis Software and Systems XVI. Astron. Soc. Pac., San Francisco, p. 127
Meier D. S., Turner J. L., Crosthwaite L. P., Beck S. C., 2001, AJ, 121, 740
Muñoz-Mateos J. C. et al., 2009, ApJ, 701, 1965
Narayanan D., Krumholz M. R., Ostriker E. C., Hernquist L., 2012, MNRAS, 421, 3127
Onodera M. et al., 2016, ApJ, 822, 42

Downloaded from https://academic.oup.com/mnras/article/485/2/2092/5315777 by guest on 13 May 2022

Pannella M., Elbaz D., Daddi E., 2013, in Wong T., Ott J., eds, Proc. IAU Symp. 292, Molecular Gas, Dust, and Star Formation in Galaxies. p. 289
Peng C., 2010, in American Astronomical Society Meeting Abstracts #215. p. 578
Pérez-Montero E., Contini T., 2009, MNRAS, 398, 949
Pettini M., Pagel B. E. J., 2004, MNRAS, 348, L59 (PP04)
Pilyugin L. S., Thuan T. X., 2005, ApJ, 631, 231 (PT05)
Popping G., Somerville R. S., Trager S. C., 2014, MNRAS, 442, 2398
Popping G., Somerville R. S., Galametz M., 2017, MNRAS, 471, 3152
Rémy-Ruyer A. et al., 2014, A&A, 563, A31
Riechers D. A. et al., 2019, ApJ, 872, 7
Rigopoulou D., Pereira-Santaella M., Magdis G. E., Cooray A., Farrah D., Marques-Chaves R., Perez-Fournon I., Riechers D., 2018, MNRAS, 473, 20
Rodighiero G. et al., 2011, ApJ, 739, L40
Sage L. J., Salzer J. J., Loose H.-H., Henkel C., 1992, A&A, 265, 19
Saintonge A. et al., 2012, ApJ, 758, 73
Saintonge A. et al., 2013, ApJ, 778, 2
Sanders R. L. et al., 2015, ApJ, 799, 138
Sandstrom K. M. et al., 2013, ApJ, 777, 5
Santini P. et al., 2014, A&A, 562, A30
Sargent M. T., Béthermin M., Daddi E., Elbaz D., 2012, ApJL, 747, L31
Sargent M. T. et al., 2014, ApJ, 793, 19
Schruba A. et al., 2012, AJ, 143, 138
Scoville N. et al., 2014, ApJ, 783, 84
Scoville N. et al., 2017, ApJ, 837, 150
Steidel C. C. et al., 2014, ApJ, 795, 165
Storey P. J., Zeippen C. J., 2000, MNRAS, 312, 813
Strazzullo V. et al., 2013, ApJ, 772, 118
Strazzullo V. et al., 2016, ApJL, 833, L20
Strazzullo V., et al., 2018, ApJ, 862, 64
Tacconi L. J. et al., 2008, ApJ, 680, 246
Tacconi L. J. et al., 2013, ApJ, 768, 74
Tacconi L. J. et al., 2018, ApJ, 853, 179
Tan Q. et al., 2014, A&A, 569, A98
Tomczak A. R. et al., 2014, ApJ, 783, 85
Tremonti C. A. et al., 2004, ApJ, 613, 898
Valentino F. et al., 2015, ApJ, 801, 132 (V15)
Valentino F. et al., 2016, ApJ, 829, 53
Walter F. et al., 2007, ApJ, 661, 102
Walter F. et al., 2014, ApJ, 782, 79
Wilson C. D., 1995, ApJ, 448, L97
Wolfire M. G., Hollenbach D., McKee C. F., 2010, ApJ, 716, 1191
Yang C. et al., 2017, A&A, 608, A144
Yoshikawa T. et al., 2010, ApJ, 718, 112
Zahid H. J., Dima G. I., Kudritzki R.-P., Kewley L. J., Geller M. J., Hwang H. S., Silverman J. D., Kashino D., 2014, ApJ, 791, 130

This paper has been typeset from a TEX/LATEX file prepared by the author.

Downloaded from https://academic.oup.com/mnras/article/485/2/2092/5315777 by guest on 13 May 2022